










Cite this: *Environ. Sci.: Adv.*, 2024, 3, 1564

Impacts of biochar and slag on carbon sequestration potential and sustainability assessment of MgO-stabilized marine soils: insights from MIP analysis†

Chikezie Chimere Onyekwena, ^{ab} Qi Li, ^{*ab} Yong Wang, ^{ab}
Ishrat Hameed Alvi, ^{ab} Yunlu Hou, ^{ab} Chima Finnian Ukaomah ^c
and Theogene Hakuzweyezu ^{ab}

Mineral carbonation is a promising strategy for mitigating carbon emissions and combating climate change. This study investigates the efficacy and sustainability of MgO-based stabilization techniques for soft marine soils, incorporating supplementary cementitious materials (SCMs) such as biochar and slag. A combination of laboratory experiments and rigorous analyses was utilized to elucidate the complex interplay between the additives and their impacts on soil hydraulic characteristics, carbon sequestration potential, embodied energy, and economic viability. Mercury intrusion porosimetry (MIP) was employed to characterize pore structure changes induced by carbonation, while X-ray diffraction (XRD) and scanning electron microscopy (SEM) were used to correlate mineral formations. The results indicate that MgO–biochar-treated soils exhibit enhanced soil air content, pore connectivity, and carbon sequestration efficiency compared to MgO–slag-treated soils, exhibiting reduced pore volumes and limited CO₂ diffusion. Integrating biochar with MgO enhanced brucite and nesquehonite precipitation due to biochar's porous structure and functionalized surface area, facilitating gas diffusion and nucleation for mineral formation. Sustainability assessments highlight the environmental and economic trade-offs, positioning MgO–biochar and MgO–slag combinations as cost-effective and environmentally friendly alternatives. This research provides theoretical guidance for sustainable soil stabilization and efficient CO₂ mineralization, offering valuable insights for researchers, practitioners, and policymakers addressing climate change challenges.

Received 27th March 2024
Accepted 2nd September 2024

DOI: 10.1039/d4va00095a

rscl.li/esadvances

Environmental significance

The environmental significance of soil stabilization with magnesia, incorporating waste-derived supplementary cementitious materials such as biochar or slag, extends beyond mere structural reinforcement. These additives play pivotal roles in influencing carbon sequestration potential and bolstering the mechanical performance of weak soils, thus presenting crucial implications for climate change mitigation and sustainable infrastructure development. Of particular significance are the insights into the intricate pore structure variations induced by carbonation, highlighting the dynamics of carbon diffusion and mineralization in stabilized soils. This holistic approach to soil stabilization using eco-friendly alternatives not only reduces carbon emissions but also promotes environmental resilience, laying the groundwork for sustainable development in the face of climate uncertainty.

1. Introduction

In response to the imperative outlined by the Intergovernmental Panel on Climate Change (IPCC) for mitigating carbon emissions and leveraging carbon dioxide (CO₂) resources to combat climate change, carbon capture utilization and storage (CCUS) technologies have emerged as vital strategies.^{1–3} Among these, mineral carbonation, which involves the chemical conversion of CO₂ into stable carbonates through reactions with cations like Mg²⁺ and Ca²⁺, stands out as a promising approach for safe and permanent CO₂ storage. This technique also aligns

^aState Key Laboratory of Geomechanics and Geotechnical Engineering, Institute of Rock and Soil Mechanics, Chinese Academy of Sciences, Wuhan 430071, China. E-mail: melbergconsult@gmail.com; qli@whrsm.ac.cn; wangyong@whrsm.ac.cn; cognitive_cleet@outlook.com; luuhou6@outlook.com; thakuzweyezu@gmail.com; Fax: +86-27-87198967; Tel: +86-27-87198126

^bUniversity of Chinese Academy of Sciences, Beijing 100049, China

^cDepartment of Energy and Mineral Engineering, The Pennsylvania State University, University Park, PA, USA. E-mail: cfu5036@psu.edu

† Electronic supplementary information (ESI) available. See DOI: <https://doi.org/10.1039/d4va00095a>



with the broader sustainability goals by potentially reducing the carbon footprint of construction projects.

Recent advancements have identified the efficacy of magnesium oxide (MgO) cement, particularly light-burned MgO, in addressing challenges associated with soft soil treatment, including dredged marine soil (DMS).^{4–6} DMS, characterized by its high compressibility and low shear strength, poses significant challenges to construction projects, necessitating effective stabilization techniques.⁷ Compared to conventional ordinary Portland cement (OPC) or lime, MgO-based formulations offer superior environmental performance and durability.^{6,8,9} Notably, MgO's pozzolanic properties and propensity for carbonation present opportunities for significant CO₂ sequestration during soil stabilization processes, with the added benefits of low-temperature production and rapid strength development.^{4,10} However, the widespread adoption of MgO-based stabilization faces hurdles related to its CO₂ footprint, micro-crack formation, and inefficient carbonation mechanisms.^{11,12} Rapid reactions between MgO and CO₂ under high-pressure carbonation curing can lead to micro-crack initiation, compromising mechanical performance.^{14,13} Additionally, the formation of bulky hydration and carbonation products inhibits CO₂ diffusion within the cementitious matrix, resulting in unreacted MgO residues and suboptimal carbonation efficiency.¹⁴

Supplementary cementitious materials (SCMs) such as slag, a by-product of steel production, have shown potential as viable additives to enhance the performance of MgO-based formulations while reducing environmental impact and eliminating the need for landfill space.¹⁰ Studies have demonstrated that incorporating SCMs improves particle packing and overall performance, leading to reduced CO₂ emissions and enhanced cost efficiency.^{15,16} Similarly, biochar, derived from biomass pyrolysis, offers a sustainable solution with negative net carbon footprints and versatile applications in soil stabilization.^{17–21}

Despite the recognized benefits of biochar and slag, their roles in facilitating CO₂ diffusion and mineralization within MgO-treated soils remain underexplored. Previous studies have focused primarily on mechanical behavior and CO₂ absorption potential, overlooking diffusion flow mechanisms and sustainability assessments.^{8,22} Moreover, Chen *et al.* reported that factors such as soil air content (SAC) and soil microstructure affect gas diffusion in stabilized soils and stressed the need to investigate the influence of pore characteristics on gas diffusion.²³ Experimental techniques such as mercury intrusion porosimetry (MIP) offer insights into the pore structure variations induced by carbonation but have yet to be fully utilized in characterizing carbonated MgO-treated soils containing SCMs.^{24,25} Furthermore, investigations on the sustainability assessment of these types of stabilized soils are still lacking.

In this study, we employ MIP to experimentally characterize carbonation-induced pore structure variations and correlate the results with mineral formations observed using X-ray diffraction (XRD) and scanning electron microscopy (SEM). Additionally, a holistic feasibility and sustainability assessment of these stabilization techniques in terms of embodied energy, carbon emissions, and cost-effectiveness was conducted. By

investigating the impact of biochar and slag on CO₂ diffusion and mineralization in MgO-treated soils, we aim to provide theoretical guidance for sustainable soil stabilization and efficient CO₂ mineralization. Integrating these sustainability considerations into our experimental results highlights the practical significance of the findings for real-world applications.

2. Materials and methods

2.1. Materials, specimen preparation, and mix composition

The key raw materials include dredged marine soil, light calcined MgO, biochar, and slag. The marine soil was obtained from Hangzhou Bay in Zhejiang Province, China.²² The MgO was sourced from Sinopharm company, while the biochar and slag were locally supplied. Biochar was produced from wheat straw biomass. The compositions of the raw materials determined *via* X-ray fluorescence (XRF) are presented in the ESI material (Table S1),[†] while Fig. S1[†] illustrates the grain size distribution determined using a laser particle analyzer.

The main mineral constituents of the different raw materials are presented in Fig. S2.[†] The marine soil is mainly composed of quartz and gismondine, consistent with the findings by Li *et al.*²⁶ The MgO binder predominantly contains periclase. Biochar primarily consists of quartz, as indicated by Table S1,[†] where SiO₂ is the dominant component. Unlike soil, MgO, and biochar, which have distinct, sharp peaks corresponding to their well-ordered atomic planes, slag exhibits a broad, diffuse hump or halo in the XRD pattern with no distinct or sharp peaks, suggesting it is predominantly amorphous. This observation aligns with the report by Lang *et al.*²⁷ However, the XRF analysis results presented in Table S1[†] show that slag is mainly composed of CaO, SiO₂, and Al₂O₃, which are important constituents for pozzolanic reactions.

The natural DMS was treated with 15 wt% MgO based on the dry soil mass, in accordance with recommendations from previous research,^{11,28} which deemed it suitable for stabilizing soft soils, denoted as M15. Samples with MgO replacement by 5 wt% and 7.5 wt% biochar are denoted as M10-B5 and M7.5-B7.5, respectively. At the same time, those replaced with 5 wt% and 7.5 wt% slag are represented as M10-G5 and M7.5-G7.5, respectively. The marine soil was mixed with the different admixtures and homogenized for 5 minutes. Subsequently, a pre-determined amount of distilled water, calculated based on compaction tests, was added and mixed for an additional 5 minutes. The soil samples were placed in cylindrical moulds (\varnothing 50 mm \times H 100 mm) and compacted to the maximum dry density.^{8,11} The samples were sealed using plastic bags and preconditioned for the first 24 h at 20 ± 2 °C temperature and 95% relative humidity before being subjected to 6 h carbonation under 99.9% CO₂ concentration and 0.2 MPa CO₂ pressure conditions. The natural soil was maintained under ambient curing conditions for 28 d.

The compaction properties of the various mix designs, such as maximum dry density (γ_{dmax}), optimum moisture content (W_{opt}), void ratio (e), and porosity (n), including the unconfined compressive strength (UCS) and CO₂ uptake after 6 hours of carbonation, which were reported in an earlier study,²² are



summarized in Table S2.† The mass compositions of the samples were determined based on compaction tests, as presented in Fig. S3.†

2.2. Methodology

2.2.1. Soil air content. The soil air content (SAC) was employed to understand the soil aeration and gas exchange processes. The SAC of each sample was determined based on the volumetric method expressed as the percentage ratio of air volume (V_a) compared to the total volume of voids (V_v) within the soil pores. The SACs were determined before carbonation, following standard phase relationships from the compaction test, to examine the impact of the additives on the stabilized soils in their natural state.

$$\text{SAC}(\%) = \frac{V_a}{V_v} \times 100\% \quad (1)$$

2.2.2. Mercury intrusion porosimetry. The mercury intrusion porosimetry (MIP) test was employed to investigate changes in pore structure, pore size distribution, and flow characteristics of the treated soil. The relationship between the pore diameter D (μm) and applied pressure P (MPa), assuming cylindrical pores, is modeled using the Washburn equation,²⁹ which describes the dynamics of capillary flow and has been adopted in characterizing the pore size distribution of stabilized soils (e.g., Cai *et al.*):³⁰

$$D = \frac{-4T \cos \theta}{P} \quad (2)$$

where T represents the surface tension of mercury (0.485 N m^{-1}), and θ is the mercury contact angle (130°).

Before the MIP test, the experimental samples were cut into approximately 1 cm cubes and polished on all surfaces to inhibit surface irregularities. The samples were then subjected to 2 hours of vacuum drying at 60 °C to expel moisture and volatiles and then cooled to room temperature in a desiccator. The MIP experiment was performed with a MicroActive Auto-Pore V 9600 mercury intrusion porosimeter, capable of analyzing pore sizes within the range of 3 nm to 800 μm .

Diffusion-controlled processes are crucial in characterizing the accessibility of reactants to active sites in porous media. Consequently, the tortuosity factor, defined as the ratio of the intrinsic to the effective transport properties accounting for the increased path length that fluid must travel through the porous material, is used to measure the efficiency of gas diffusion through the soil pore networks.^{31,32} The tortuosity factor τ for each sample was determined using the following relationship:

$$\tau = \frac{D_b \varepsilon}{D_{\text{eff}}} \quad (3)$$

where D_b is the intrinsic diffusion coefficient in bulk fluid, D_{eff} is the effective diffusion coefficient, and ε is the pore volume fraction calculated as the ratio of the volume of pores from the MIP to the total volume of the sample. The intrinsic coefficient D_b for mercury, used in the tortuosity factor equation, is a pre-defined value embedded within the software of the MIP

equipment. This coefficient is not directly measured but rather is an integral part of the instrument's software, which also incorporates other essential parameters for analyzing pore size distribution and pressure data. The effective diffusion coefficient D_{eff} was determined using data obtained from the MIP test by correlating the pore structure characteristics with the diffusion process through the porous medium.

In addition, the mercury saturation was determined in line with the GB/T 29171-2012 standard. This involves calculating the change in mercury volume at consecutive pressure steps, adjusting by a correction factor, and normalizing by the total pore volume, as shown in eqn (4).

$$\Delta S_{\text{Hg}} = \frac{(V_{i+1} - V_i) - (V_{k_{i+1}} - V_{k_i})\alpha}{V_p} \times 100 \quad (4)$$

where ΔS_{Hg} is the change in degree of saturation (%); V_{i+1} is the volume at pressure p_{i+1} (mL); V_i is the volume at pressure p_i (mL); $V_{k_{i+1}}$ is the cumulative volume at the next pressure step (mL); V_{k_i} is the cumulative volume at the current step (mL); α is the correction factor; V_p is the pore volume (mL). The correction factor α was determined based on the calibration of the instrument, as per the manufacturer's specifications, to ensure accurate adjustment of the measured volume.

The cumulative mercury saturation S_{Hg} is then determined by summing these values across all pressure steps as follows:

$$S_{\text{Hg}} = \Delta S_{\text{Hg}} \quad (5)$$

The pore size distribution, pore volume, porosity, and tortuosity factor obtained from the MIP exploration were used to characterize the pores in the samples.

2.2.3. Microstructural analysis. The specimens obtained from crushed samples used in strength testing were freeze-dried using a vacuum drier to halt hydration in preparation for X-ray diffraction (XRD) and scanning electron microscopy (SEM). Post-drying, the samples were ground to pass through a 75 μm sieve before being subjected to XRD analysis. XRD analysis was carried out using a Bruker D8 X-ray spectrometer with Cu K α radiation at 40 kV and 40 mA, scanning from 5° to 80° 2θ at a rate of 2° 2θ /step. Subsequently, the XRD patterns were analyzed using MDI Jade 6.0 software to identify and quantify the crystalline phases present in the samples. This software allowed for accurate matching of diffraction peaks to standard mineral databases, facilitating the identification of various minerals. Before SEM examination, the dried samples were affixed to aluminum ends using double-sided adhesive carbon disks and coated with gold. The microstructure provides insights into the morphology of hydration and carbonation products within the analyzed samples.

2.2.4. Sustainability assessment. A comprehensive sustainability analysis was conducted to investigate the economic, environmental, and energy-related impacts of adopting various additives for marine soil stabilization. This analysis evaluated the cost-effectiveness, carbon footprint, and embodied energy of different strategies. Eqn (6)–(8) were used to quantify these indicators for each soil stabilization method.



$$CEE = \sum_{i=1}^N W_i \cdot IEE^i + D \cdot IEE^d + E \cdot IEE^e \quad (6)$$

$$CCO_2 = \sum_{i=1}^N W_i \cdot ICO_2^i + (W_t \cdot ICO_2^{dt} + H_m \cdot ICO_2^{dm}) + E \cdot ICO_2^e \quad (7)$$

$$CC = \sum_{i=1}^N W_i \cdot IC^i + D \cdot IC^d + E \cdot IC^e \quad (8)$$

where CEE, CCO₂, and CC are the cumulative embodied energy, cumulative CO₂ emissions, and cumulative cost of raw materials per tonne of treated soil. IEEⁱ, ICO₂ⁱ, and ICⁱ are the individual embodied energy, CO₂ emissions, and cost per unit of raw materials, respectively. IEE^d, ICO₂^d, and IC^d are the embodied energy, CO₂ emissions, and cost per unit of diesel, respectively; where ICO₂^{dt} and ICO₂^{dm} are CO₂ emissions per unit of diesel for transport and machine operations. W_i represents weight per unit of raw materials *i*, *N* is the number of raw material types, W_t denotes the factored weight of materials, H_m is the hours of machine operation, *E* is the electricity used, and *D* is the diesel for transport and machine operations. All the defined terms, parameters, and units are properly detailed in the ESI material.†

Data used in the sustainability analysis were obtained from experimental measurements, literature reviews, and industry standards, as presented in Table S3.† Furthermore, Table S3† and the sustainability assessment tool in the ESI material† contain links to all references used in the analysis. The system boundary employed for the impact assessment of the different samples is illustrated in Fig. 1. The figure presents the raw materials and processes leading to the manufacture of

a functional unit of 1 tonne of treated marine soil, along with its potential applications. Life cycle assessment (LCA) principles were employed to ensure a holistic evaluation of sustainability factors per the International Organization for Standardization.^{3,10,33}

The MgO used in this study was assumed to be obtained from the calcination of magnesite (MgCO₃ → MgO + CO₂). The requisite inventories, encompassing emissions data primarily stemming from the production of MgO, were sourced from the global database Ecoinvent v3.4. Global average emissions data used for diesel and electricity (employed in various stages, including raw materials extraction and transportation, grinding, and machine operation during curing) were adopted.¹⁰

2.2.5. Sensitivity analysis. Sensitivity analyses were conducted to assess the influence of key parameters on CO₂ emissions and cost. The sensitivity analysis assumed variations up to 50% decrease or increase in materials and processes on cost and CO₂ emissions. For each selected sample, the estimated values of all parameters were kept constant except for the material of interest being assessed. The quantity of the material of interest was adjusted by either −50% or +50% and added to the original value of that material.

This procedure was used to simulate the impact of a decrease or increase in the material quantity on the cumulative output of the various indicators considered. For example, when the quantity of material is multiplied by −50% and added to the original value, it simulates a 50% decrease. In contrast, when the quantity is multiplied by +50% and added to the original value, it simulates a 50% increase. Adding this adjusted value to the estimated values of other parameters, which are kept constant, reveals the impact of varying that particular material on the cumulative indicator. Comprehensive details on the

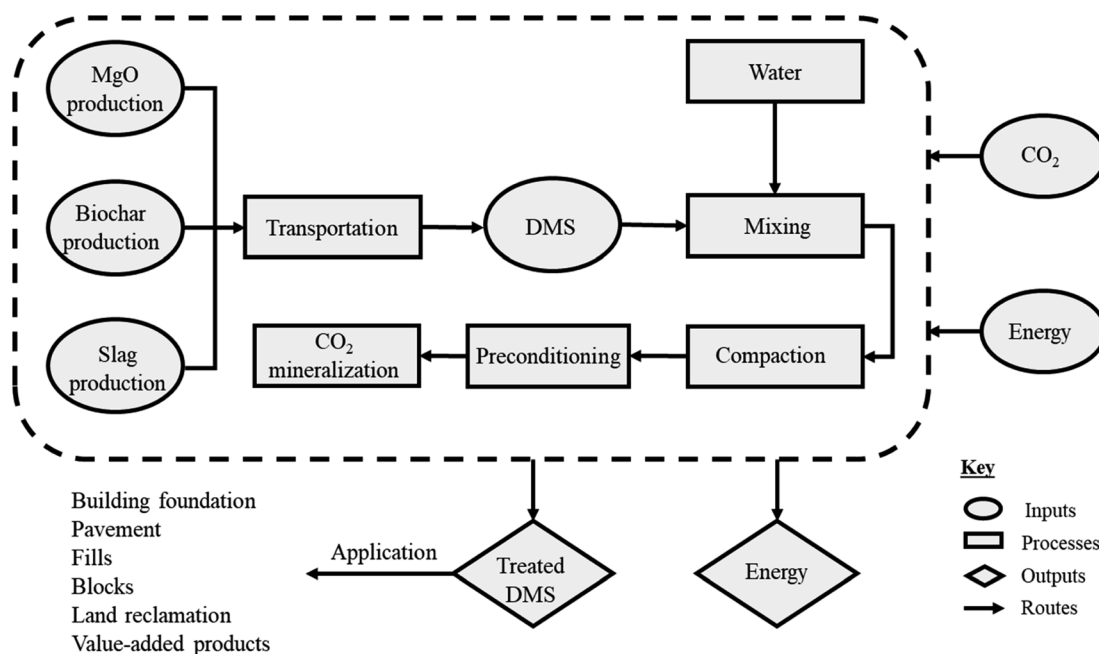


Fig. 1 System boundary for the environmental assessment of the various samples.



sustainability impact assessments and the associated calculations can be found in the ESI material.†

3. Results and discussion

3.1. Soil air content

Soil air content (SAC), representing the air volume within the pore spaces of soil, plays a vital role in regulating gas transport through soils.²³ The SAC results for the different mix designs are presented in Fig. 2. Among the samples, M10-B5 exhibited the highest SAC at 19.60%, indicating increased pore spaces and enhanced soil aeration. Conversely, the untreated soil sample displayed the lowest SAC at 9.26%, reflecting its natural state. Notably, the biochar-treated samples, M10-B5 and M7.5-B7.5, demonstrated higher SAC compared to their slag-treated counterparts, M10-G5 and M7.5-G7.5, suggesting a potential influence of biochar on pore connectivity. The observed variations in SAC highlight the impact of different additives on soil structure and gas diffusion dynamics. The disparity in SAC between the M10-B5 and M7.5-B7.5 samples is attributed to the water retention properties of biochar, as indicated by the moisture content data presented in Table S2.† Specifically, the higher moisture content in the M7.5-B7.5 sample led to a 3% decrease in SAC compared to the M10-B5 sample, highlighting the potential influence of biochar on soil permeability and aeration.

These findings highlight the complexity of soil-air-water interactions and emphasize the importance of understanding the effects of additives on soil properties. Therefore, subsequent investigations employing techniques such as MIP, XRD, and SEM will provide insights into the mechanisms underlying changes with respect to carbonation to guide future applications of soil stabilization additives.

3.2. Mercury intrusion porosimetry investigation

Fig. 3 illustrates the cumulative pore volume and pore-size distribution for the natural soil after 28 d ambient curing and

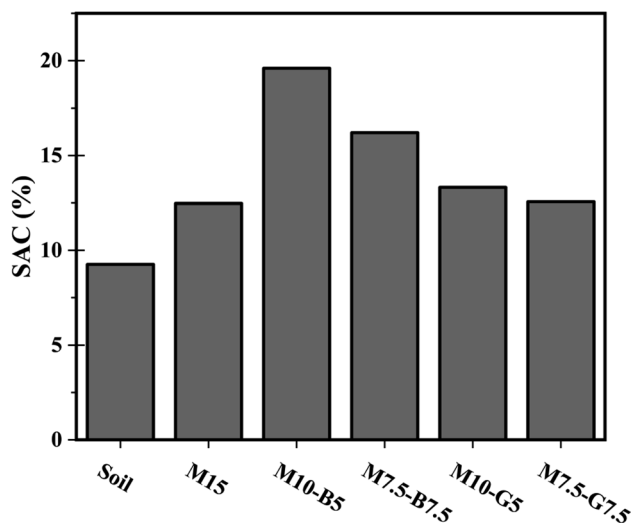


Fig. 2 Soil air content of different samples.

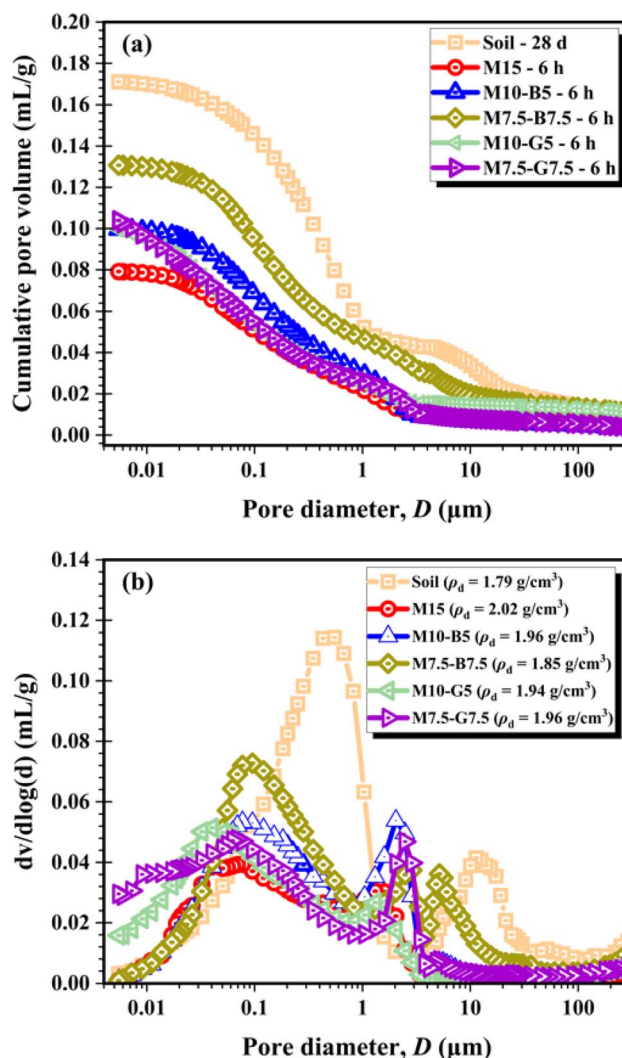


Fig. 3 (a) Cumulative pore volume and (b) pore-size distribution of the different samples.

the treated soils after 6 h of CO₂ curing. Fig. 3a shows that the M15 sample containing 15 wt% MgO experienced a significant decrease in pore volume. Substituting MgO with biochar resulted in increased pore volume compared to using slag.

Pore diameters are typically categorized as macropores (>50 nm) and mesopores (ranging from 2 to 50 nm).³⁴ As shown in Fig. 3b, pore size distribution curves for all soil samples exhibit peaks in the macropore and mesopore regions. However, the treated soils are predominantly characterized by mesopores, whereas macropores dominate the untreated soil. The difference between the behavior of the untreated soil curve compared to the treated soils can be attributed to the sequential precipitation of hydration and carbonation products in the treated soils due to the presence of MgO-based binders. The precipitated products, formed initially through hydration and subsequently through carbonation, fill up void spaces and significantly reduce the porosity of the treated soil samples, thereby highlighting the impact of CO₂ curing on the treated soil samples.



Unlike the bare soil, which exhibits a wide disparity in macropore volume, all treated soil samples show evidence of hydration and carbonation product precipitation. This results in less dominant macropore development and convergence towards the mesopore region ($\sim 0.01 \mu\text{m}$ pore diameter) at 0.10 mL g^{-1} cumulative pore volume, except for samples M15 and M7.5-B7.5 (Fig. 3a). The M15 curve converges at a lower cumulative pore volume (0.08 mL g^{-1}), likely due to higher MgO content, leading to increased formation of hydration and carbonation products during carbonation. Conversely, the M7.5-B7.5 curve converges at a higher cumulative pore volume (0.13 mL g^{-1}), attributed to the reduced MgO content and increased biochar content, which is highly porous nature.²⁰

The threshold pressure, an established concept in MIP analysis, refers to the pressure at which mercury begins to intrude into the smallest accessible pores of the material. This pressure indicates the flow initiation within the pore network. The threshold pressure is determined from the MIP curve at the point where a significant increase in mercury intrusion volume is observed.³⁵ This corresponds to the diameter of the smallest dominant pore size, as shown in Fig. S4.† Understanding this value is crucial for assessing the pore structure and connectivity, which directly influence the flow initiation and permeability characteristics of the stabilized soils. Analysis reveals that less pressure is required for flow within the pore networks of untreated soil (Fig. S4a†) compared to the stabilized soils, indicating enhanced mechanical performance. The potential precipitation of hydration and carbonation products in stabilized soils reduced their pore sizes due to the filling and cementing effect of the formed products, thereby resulting in reduced porosity and increased pressure for flow. Notably, the M10-B5 sample exhibits a theoretical pressure similar to that of the M15 sample. This observation suggests that despite the lower MgO content in the M10-B5 sample, equivalent pressure is required for flow initiation in both samples, implying comparable formation of carbonation products.

The plot illustrating the product of net intrusion volume ($V_c - V_{th}$) and pore diameter cubed (D^3) against the pore diameter, is depicted in Fig. S5.† V_c represents the cumulative intrusion volume at a specific pressure, while V_{th} is the cumulative intrusion volume at the threshold pressure. The maxima of the curve in Fig. S5† indicate D_{max} , the pore diameter (μm) at maximum hydraulic conductance within the pore network.³⁵ It is noteworthy that D_{max} is influenced by the threshold pressure. Analysis reveals a significant decrease in the D_{max} of the M15 soil sample compared to the natural soil, concurrent with an increase in P_{th} due to the elevated pressure requirement for flow through smaller pores. Interestingly, both the M10-B5 and M15 samples exhibit equivalent D_{max} , suggesting the possible precipitation of similar hydration and carbonation products within the samples. In comparison, the biochar mixtures required lower pressure compared to those containing slag (Fig. S4†), with slag mixtures displaying smaller D_{max} . This phenomenon could be attributed to the filling effect of slag, resulting in reduced pore size and necessitating higher pressure for flow within the pore network. Overall, the observed inverse relationship between D_{max} and the threshold pressure implies

that samples with smaller D_{max} require higher threshold pressures, suggesting the need for higher CO_2 pressure for effective carbonation of slag-containing samples.

The mercury saturation degree of the samples is depicted in Fig. 4. According to Cai *et al.*, pore diameters of $0.01 \mu\text{m}$ and $10 \mu\text{m}$ represent thresholds distinguishing intra-aggregate and inter-aggregate pores, and inter-aggregate and air pores, respectively. Additionally, inter-aggregate pores can be categorized into small inter-aggregate pores ($0.01\text{--}0.1 \mu\text{m}$) and large inter-aggregate pores ($0.1\text{--}10 \mu\text{m}$).³⁰ While this categorization is a convention used in the literature, it provides a useful framework for analyzing the pore structure in the present study.

Fig. 4 illustrates that saturation progresses normally within the large pores ($\geq 0.1 \mu\text{m}$). However, as the pores approached the small range ($< 0.1 \mu\text{m}$), saturation levels decreased in the slag mixtures, failing to achieve 100% saturation compared to other mixtures. This indicates that CO_2 diffusion occurs more rapidly during carbonation in the plain MgO and MgO–biochar samples than in the MgO–slag samples. Inadequate CO_2 diffusion in the samples containing slag may compromise carbonation efficiency, leading to inefficient CO_2 mineralization and utilization of the incorporated binders.

In the pore volume comparison of different samples (Fig. 5), variations in pore volumes across distinct size ranges were observed, shedding light on the intricate pore structures influenced by biochar and slag additives in MgO-stabilized soil after carbonation. Notably, the carbonation process, driven by the rapid diffusion of CO_2 , has implications for pore volumes across various size ranges. The analysis encompassed pore sizes ranging from $0.0028 \mu\text{m}$ to $50 \mu\text{m}$. The untreated soil generally showed high pore volumes across all regions.

Among the examined stabilized soil samples, M10-G5 and M7.5-G7.5 exhibited reduced pore volumes in the larger size ranges ($0.05\text{--}0.1 \mu\text{m}$, $0.1\text{--}1 \mu\text{m}$, and $10\text{--}50 \mu\text{m}$). This behavior aligns with the compaction test results indicating low porosity, void ratio, and SAC. It suggests a potential limitation on CO_2 diffusion and storage capacities in these larger size ranges

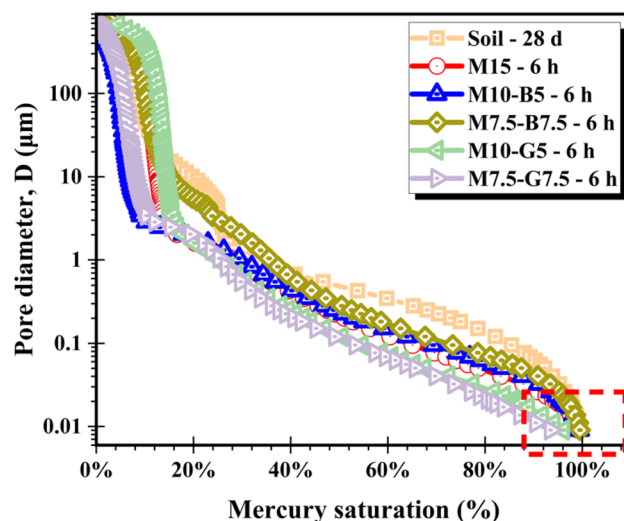


Fig. 4 Mercury saturation degree of the different samples.



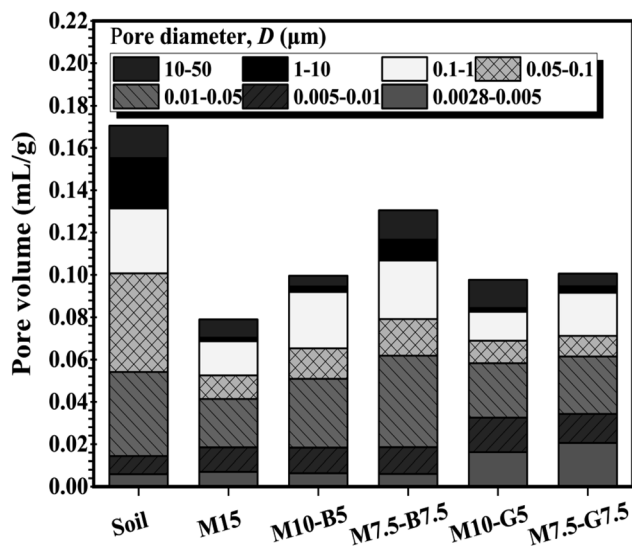


Fig. 5 Pore volume comparison of different samples.

(macropores), potentially constraining the formation of hydration and carbonation products in lower pore diameter ranges. Conversely, M10-B5 and M7.5-B7.5 demonstrated reduced pore volumes in smaller pore size ranges (0.0028–0.005 μm and 0.005–0.01 μm). This could be attributed to the accelerated diffusion of CO_2 and the precipitation of hydration and carbonation products in these micropores, potentially enhancing surface reactivity and modifying adsorption characteristics. M15 displayed a unique pattern with reduced pore volumes. These observations highlight the intricate interplay between additives, carbonation kinetics, and resulting pore structures.

Fig. 6 portrays the porosity plot of various samples before and after curing, offering insights into the structural alterations induced by MgO, biochar, and slag additives. While the natural soil's porosity slightly increases from 29.93% to 30.57% after 28 days of ambient curing, potentially due to void spaces from

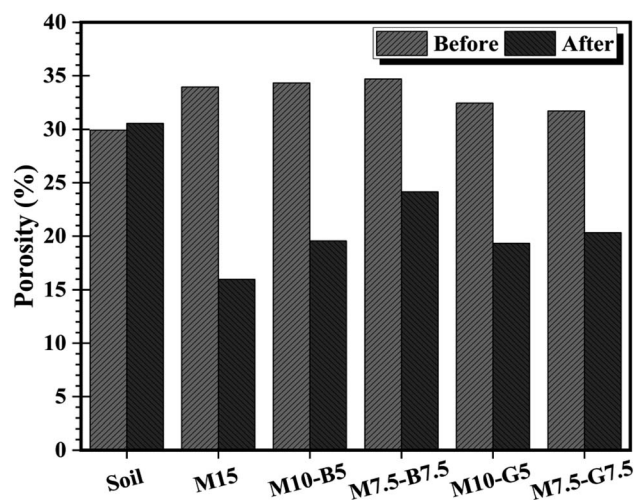


Fig. 6 Porosities of samples before and after curing.

moisture loss, indicating minimal structural changes, the stabilized soils exhibit a notable decrease in porosity post-carbonation, despite moisture loss. This reduction suggests significant modifications in pore structure and potential enhancements in soil compactness, indicative of a densification effect and potential soil strength improvement. The observed variations in porosity after curing align with alterations in pore volumes observed in Fig. 5.

The summary of pore structure characteristics presented in Table 1 offers a comprehensive overview of the impact of MgO, biochar, and slag additives on the microscopic features of the samples. The M15 sample exhibited an increase in density from 1.79 g cm^{-3} to 2.02 g cm^{-3} after carbonation, indicating enhanced soil compaction. MgO–biochar samples (M10-B5 and M7.5-B7.5) showed intermediate porosities (19.53% and 24.15%), suggesting a balance between compaction and aeration. MgO–slag samples (M10-G5 and M7.5-G7.5) demonstrated porosities of 19.33% and 20.33%, indicating potential densification effects and improved soil strength.

The alterations in density and pore throat size, particularly in the stabilized soils, indicate structural modifications and influence on fluid flow dynamics, suggesting potential enhancements in soil compactness. The total pore volume and area provide insights into the overall void spaces within the stabilized soils, showcasing variations in structural characteristics. The tortuosity factor reflects diverse fluid flow dynamics, with MgO, biochar, and slag additives influencing the ease of fluid movement through the soil matrix. The D_{50} and P_{50} values offer insights into the median pressure and particle size distribution, indicating potential variations in the pore network characteristics. The findings show that P_{50} increases with decreasing D_{50} , reflecting the mechanical performance of the soil samples.

The findings contribute to understanding the mechanisms governing gas transport and storage in MgO-stabilized soil, paving the way for informed applications in engineering and environmental contexts. Further investigations into the specific contributions of macropores and micropores to soil properties and functions would be valuable for refining our comprehension of these complex systems.

3.3. X-ray diffraction

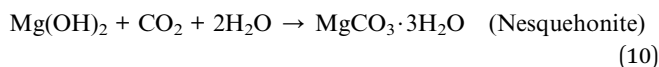
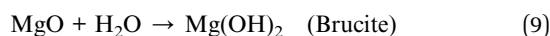
The XRD spectra elucidating the mineralogical composition of the stabilized soil samples and the implications for pore structure evolution and carbon storage are presented in Fig. S6.† The predominant mineral in the natural soil was quartz, constituting a large portion of the mineral phase, followed by gismondine. This is consistent with the study by Li *et al.* on marine soil treatment.²⁶ Upon stabilization with MgO and SCMs such as biochar and slag, significant changes in mineralogical composition were observed. Samples containing MgO and biochar exhibited augmented nesquehonite and brucite formation, as evidenced by the peak intensities of the XRD patterns compared to other mineral phases. In contrast, samples containing MgO and slag precipitated calcium carbonates in addition to other minerals. This enhanced



Table 1 Summary pore structure characteristics for different samples

Sample ID	Porosity (%)	Density (g cm ⁻³)	Average pore throat size (nm)	Total pore volume (mL g ⁻¹)	Total pore area (m ² g ⁻¹)	Tortuosity factor	P ₅₀ (MPa)	D ₅₀ (nm)
Soil	30.56	1.79	149.51	0.1710	4.576	1.885	2.60	479.32
M15	15.96	2.02	78.05	0.0792	4.058	2.050	5.88	211.97
M10-B5	19.53	1.96	91.83	0.0997	4.343	2.009	5.17	241.04
M7.5-B7.5	24.15	1.85	108.88	0.1307	4.803	1.957	3.70	337.04
M10-G5	19.33	1.94	45.87	0.0996	8.686	2.012	8.58	151.11
M7.5-G7.5	20.33	1.96	37.49	0.1040	11.094	2.000	12.45	100.18

formation of hydrate and carbonate minerals has significant implications for carbon storage. Brucite precipitates nesquehonite upon exposure to atmospheric CO₂ through mineral carbonation processes, thereby contributing to long-term carbon storage in stabilized soils, as illustrated in eqn (9) and (10). The observed precipitated hydration and carbonation products align with previous studies on soft soil treatment using MgO-based binders.^{4,8}



Nesquehonite exhibits greater crystallinity when compared to other carbonation products. Its expansion in volume during formation in carbonated soils is bound to rapidly occupy the existing large pores, thereby leading to a notable reduction in porosity.³⁰ Major peaks of nesquehonite were identified at two theta 13.57°, 23.02°, 29.39°, 34.15°, and 47.11°. The variations in the crystalline nesquehonite peak intensities of the carbonated samples at 13.57°, 23.02°, and 29.39° are illustrated in Fig. 7a. M15 and M10-B5 exhibit higher nesquehonite intensities compared to other samples, consistent to the quantitative XRD (QXRD) analysis presented in Fig. 7b. The QXRD analysis provided the relative proportion of the nesquehonite mineral phase in each sample. This was accomplished using the Rietveld refinement method, which involved fitting the

experimental data to theoretical models by adjusting parameters such as lattice constants, crystallite size, and strain. The refinement process was validated using standard goodness-of-fit parameters, ensuring the accuracy of the results. When comparing the MgO–biochar and MgO–slag samples, potential interactions between pozzolans in biochar and MgO resulted in the precipitation of higher hydration products. This phenomenon subsequently led to increased carbonation products during carbonation. During hydration, MgO dissolves in H₂O, releasing Mg²⁺, part of which nucleates with OH⁻ to precipitate brucite, while the remainder reacts with the high silica content in biochar and soil (Table S1 and Fig. S2†) to precipitate magnesium silicate hydrate (M-S-H), thereby enhancing pozzolanic reactions. Upon carbonation, when in contact with or subject to CO₂, the diffused CO₂ reacts with brucite (Mg(OH)₂) to precipitate hydrated magnesium carbonates (HMCs) such as nesquehonite. The incorporation of biochar, derived from biomass pyrolysis, not only acts as a soil stabilizer but also serves as a carbon sink due to its high surface area and porosity, which enhances CO₂ adsorption and mineralization. The overall reaction mechanism of MgO hydration and carbonation leading to permanent carbon capture is summarized in eqn (9) and (10). Hence, biochar exhibits good compatibility with MgO, providing nucleation sites for increased chemical reactions due to its highly functionalized surface area and porous nature, leading to enhanced precipitation of brucite and nesquehonite.

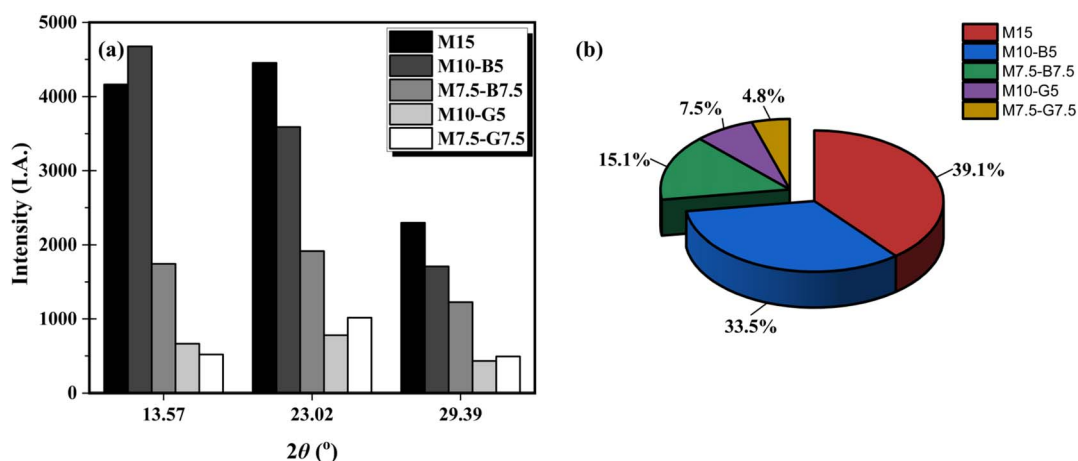


Fig. 7 Nesquehonite formations obtained from XRD analysis: (a) peak intensities, (b) Q-XRD results.



The incorporation of SCMs influenced the mineralogical composition and pore structure evolution, thus impacting soil permeability and carbonation kinetics. The low carbonate formation observed in the MgO–slag samples is a result of the reduced pore volumes observed in the macropore region (Fig. 5). Consequently, CO₂ diffusion is restricted, limiting the storage potential of the samples and leading to the formation of larger pore volumes within smaller pore diameters. These observations in mineral formations corroborate the MIP results, indicating a correlation between carbonation-induced mineral phases and alterations in pore structure.

The observed increase in nesquehonite and brucite formation in MgO and MgO–biochar samples highlights the potential for carbon storage in stabilized soils. By promoting carbonation reactions and facilitating the sequestration of atmospheric CO₂, these mineral phases contribute to the mitigation of greenhouse gas emissions and the promotion of sustainable soil management practices. The XRD analysis results, identifying the various phases and their respective positions using MDI Jade 6.0 software, are available in the XRD analysis result tab of the ESI material.† The subsequent microstructural analysis will provide more insights into the microscale effects of MgO, biochar, and slag additives on the stabilized soil.

3.4. Scanned electron microscopy

The SEM photomicrographs of the samples are shown in Fig. 8. After 28 days of ambient curing, the untreated soil revealed a landscape of soft, flaky-like particles punctuated by large pores – a testament to its initial state. Upon carbonation, significant occurrences of rod-like nesquehonite emerged in the MgO-treated soils, hinting at the intricate interplay between MgO reactivity and carbonate mineral formation. The formation of nesquehonite aligns with previous studies indicating the precipitation of well-connected carbonates, potentially leading to a denser network and reduced porosity within MgO systems.^{4,8} Intriguingly, the quality of the nesquehonite network observed in the M10-B5 sample correlated with a notable reduction in porosity, stressing the influence of biochar additives in facilitating carbonation reactions and pore structure modifications. Conversely, the M10-G5 sample showcased a denser packing attributed to the flocculation effect of slag, alongside the presence of needle-shaped aragonite, indicative of the significant CaO content inherent in slag. Notably, the MgO–biochar samples demonstrated superior nesquehonite precipitation compared to their MgO–slag counterparts, which can be potentially attributed to the diffusion channels and nucleation sites occasioned by biochar incorporation.²¹ These channels, as shown in Fig. S7,† may have facilitated the diffusion of CO₂ gas, enhancing the reactivity of MgO and promoting the formation of hydrated magnesium carbonates.

Overall, these microstructural observations offer valuable insights into the dynamic processes governing carbonation-induced mineralogical transformations in MgO-stabilized soils, highlighting the potential role of additives in modulating pore structures and influencing carbon storage mechanisms.

Given the implications of these microstructural and pore structural changes, evaluating the broader sustainability impacts of the stabilization methods is essential. Therefore, building on the experimental findings, we analyze the embodied energy, CO₂ emissions, and cost of each technique to understand their environmental and economic viability. This comprehensive evaluation considers the materials' lifecycle, from production to application, and their potential for reducing the carbon footprint of soil stabilization processes. The following section presents the sustainability assessment findings, highlighting the trade-offs and benefits of using MgO, biochar, and slag-based additives in treated marine soil.

3.5. Sustainability assessment

Fig. 9 shows the embodied energy, CO₂ emissions, and financial cost of 1 tonne of treated marine soil using MgO, biochar, and slag-based additives, estimated using eqn (6)–(8). Detailed calculations are presented in the sustainability analysis tab of the ESI material.† Fig. 9 presents a bar chart of the individual contributors (*i.e.*, soil, MgO, water, biochar, slag, electricity, and diesel) for each soil sample, summing up to their respective cumulative totals for each sustainability indicator. The embodied energy analysis reveals significant variations in energy consumption across different stabilization techniques (Fig. 9a). MgO proves to be the primary contributor to embodied energy, owing to its energy-intensive production processes. Conversely, biochar and slag incorporation exhibit lower embodied energy values, reflecting their potential as more sustainable alternatives.

The diesel consumption remains consistent across all samples, indicating a uniform energy requirement for transportation and equipment operation regardless of the specific stabilization mixture used. Similarly, the embodied energy values for soil production are relatively consistent across the samples, suggesting similar energy requirements for extracting, processing, and transporting soil materials. The energy consumed for water and electricity usage is relatively low compared to other components, contributing minimally to the overall embodied energy of the stabilization process. The findings highlight the importance of considering energy efficiency in material selection for soil stabilization applications.

The CO₂ emissions assessment (Fig. 9b) reveals insights into carbon sequestration potential and environmental impact. Negative values signify CO₂ uptake, indicating carbon capture, while positive values denote emissions. Results show substantial CO₂ uptake during the carbonation, yet MgO-treated samples (M15) exhibit the highest emissions (153.77 kg per metric ton), emphasizing the need for optimization to reduce environmental impact. Interestingly, incorporating biochar and slag leads to contrasting CO₂ emissions trends, with biochar demonstrating a notable reduction in emissions and increased carbon uptake due to its carbon sequestration potential and the negative net CO₂ emissions during production, aligning with prior findings.¹⁹ Fig. 9c highlights MgO and diesel consumption as significant cost drivers, contributing to higher production costs for the treated soil samples. In contrast, biochar and slag



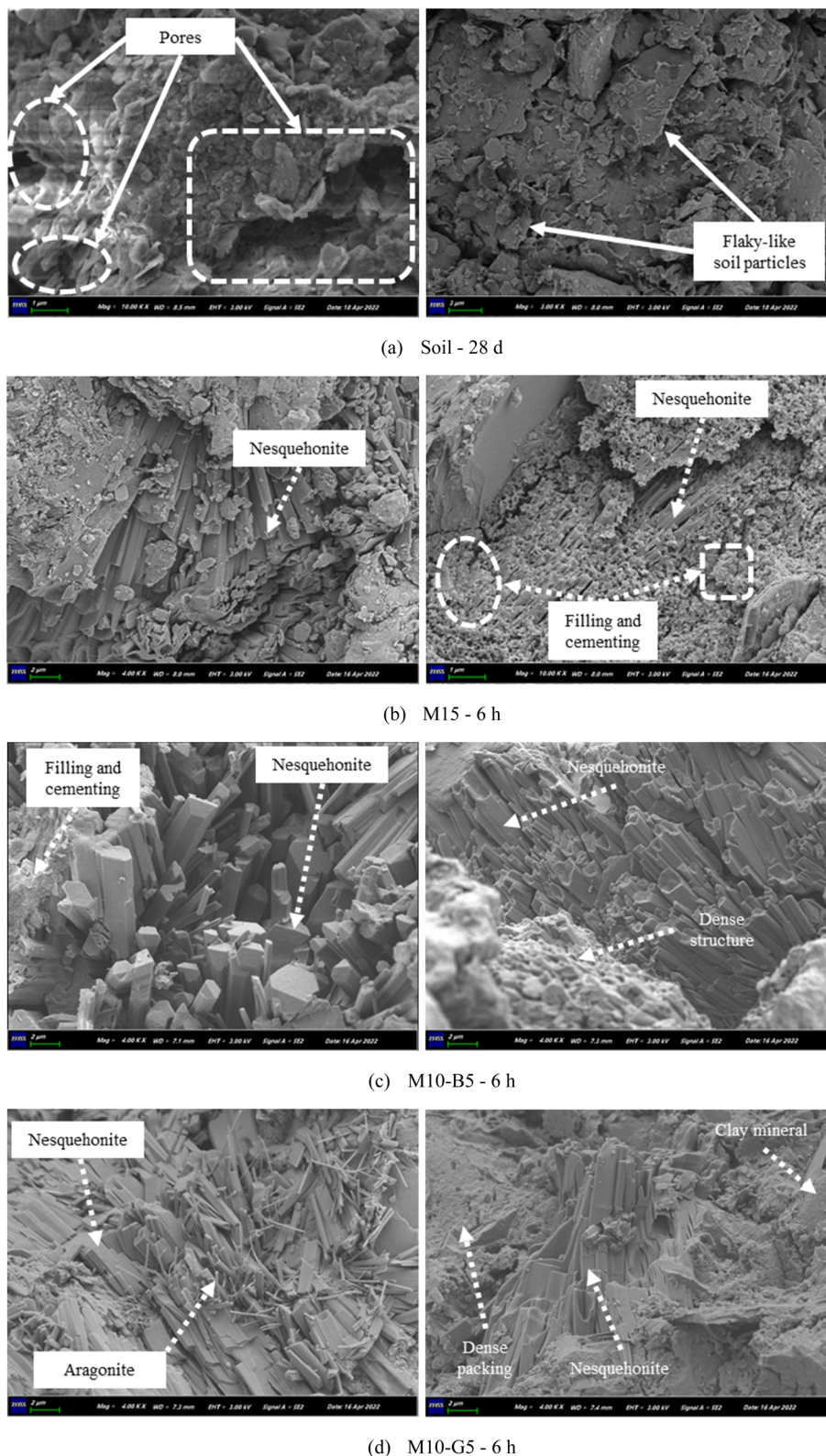


Fig. 8 Morphology of samples (a) soil – 28 d, (b) M15 – 6 h, (c) M10-B5 – 6 h, (d) M10-G5 – 6 h.

incorporation offer cost-saving opportunities, although to a certain degree, depending on the formulation and application requirements. Thus, highlighting the importance of considering costs in decision-making for soil stabilization.

To further understand the influence of key factors on cost and CO₂ emissions, sensitivity analyses were conducted using the M10-B5 and M10-G5 as a reference samples. The input parameters were independently varied by $\pm 50\%$ to assess their



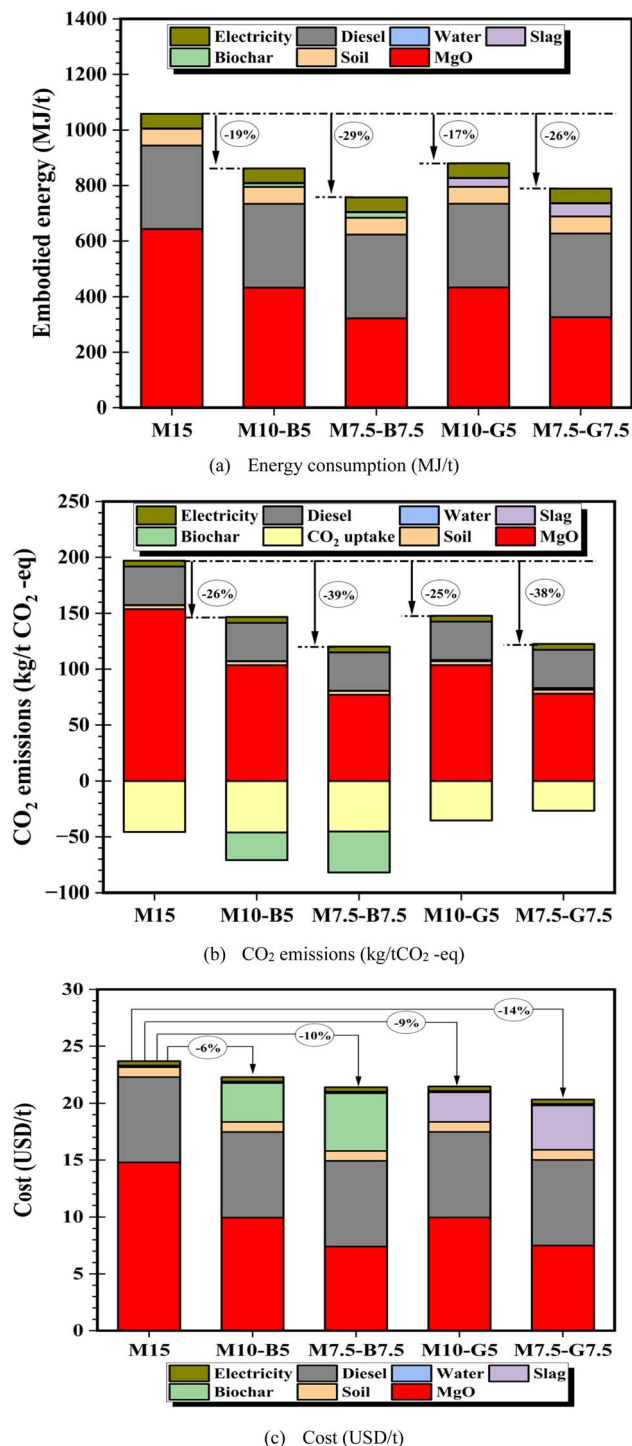


Fig. 9 (a) Energy consumption, (b) CO₂ emissions, and (c) cost analysis of the 6 h carbonated samples.

impact on cost and CO₂ emissions. MgO and diesel consumption are identified as the most sensitive factors affecting both cost (Fig. S8[†]) and CO₂ emissions (Fig. S9[†]), highlighting the need for optimization strategies to minimize environmental impact while maximizing cost-effectiveness. Additionally, biochar exhibits greater sensitivity to CO₂ emissions reduction than slag, emphasizing its potential role in mitigating greenhouse gas emissions.

Integrating these findings from the embodied energy, CO₂ emissions, and economic analyses provides a holistic understanding of the sustainability implications of different soil stabilization techniques. By considering environmental and economic factors, stakeholders can make informed decisions to promote sustainable infrastructure development and mitigate environmental impact. Overall, the sustainability assessment highlights the importance of adopting a multifaceted approach to soil stabilization, balancing environmental stewardship with economic viability to achieve long-term sustainability goals.

4. Discussion

The present study aimed to comprehensively investigate the efficacy of various soil stabilization additives, including MgO, biochar, and slag, in improving soft soil properties and their implications for carbon sequestration and sustainability. The effects of these additives on soil pore structure, carbonation-induced mineralogical changes, and environmental and economic sustainability were examined through a series of laboratory experiments and analyses.

The results revealed intriguing insights into the complex interplay between soil additives and their impacts on soil properties. Firstly, the SAC and pore structure analysis demonstrated that the incorporation of MgO, biochar, and slag additives significantly influenced soil porosity across different pore size ranges. Specifically, MgO-biochar-treated samples exhibited elevated pore volumes in inter-aggregate pores (0.01–0.05 μm), potentially enhancing surface reactivity and carbon sequestration efficiency. Conversely, MgO-slag-treated samples demonstrated reduced pore volumes in larger pores, highlighting the limitations on CO₂ diffusion and potential constraints on carbonation product formation, potentially leading to larger pore volumes within the mesopore region (0.0028–0.01 μm).

The XRD and SEM analyses provided further evidence of the influence of soil additives on mineralogical composition, with notable formations of nesquehonite and brucite in MgO-only and MgO-biochar-treated samples. In contrast, samples treated with MgO-slag exhibited low carbonation products, which is evident from the MIP exploration, suggesting that the impediment of the MgO-slag mixture to CO₂ diffusion resulted in superficial carbonation product formation. Despite these challenges, slag incorporation offers economic benefits and may find applications in specific soil stabilization scenarios. These mineralogical changes suggest the potential for enhanced carbon storage capacity in soils treated with less MgO content augmented with waste-derived biochar additives, contributing to natural resource conservation, waste management, and climate change mitigation efforts.

Moreover, the sustainability analysis reveals varying levels of embodied energy, CO₂ emissions, and costs associated with different soil stabilization techniques. MgO treatment contributed significantly to energy use, emissions, and production costs, while biochar and slag incorporation led to notable savings in these aspects. Sensitivity analyses further elucidate the influence of key factors, such as MgO and diesel



consumption, on cost and emissions, emphasizing the importance of optimizing input parameters for sustainable soil stabilization practices. Fig. S2† illustrates that the MgO binder used in this study contains a high periclase content. Therefore, utilizing waste adsorbents high in periclase, such as waste MgO refractories³⁶ or by-products from mining activities of MgCO₃ (ref. 37) can reduce cost and conserve resources. Furthermore, transitioning from the use of fossil fuels to renewable energy sources can significantly reduce energy demand and production costs.

Having explained the detailed carbon capture mechanism in Section 3.3, it is worth quantifying the carbon sequestration potential on a macro level to assess the potential carbon capture per year if this technology is deployed for the stabilization of dredged marine sediments, which would otherwise be disposed of as waste. Loudini *et al.* reported that the dredging operations for port maintenance generate about 600 million m³ of marine sediments annually (*i.e.*, 1.08 billion tonnes at a density of 1.8).³⁸ From our experiment, the CO₂ sequestration by the MgO–biochar sample averages about 45 kg per tonne.

Following the field investigation and large-scale model tests by Liu *et al.* and Cai *et al.* using MgO and CO₂ for stabilizing soft-soil highway subgrades,^{4,39} stabilizing about 20% of the 1.08 billion tonnes (*i.e.*, 216 million tonnes) using our proposed technique for land reclamation could potentially capture approximately 9.72 million tonnes of CO₂ annually. The scalability of this technology using the combination of MgO and biochar is supported by the relatively lower energy requirements and emissions associated with the binder compared to other binders.

The discussion of these findings highlights the importance of considering not only the technical efficacy but also the environmental and economic sustainability when evaluating soil stabilization techniques. This investigation contributes valuable insights by providing a comprehensive assessment of the impacts of MgO, biochar, and slag additives on soil properties and their implications for carbon sequestration and sustainability. These findings have significant implications for the development of sustainable soil management strategies and highlight the potential of biochar and slag as alternative additives for enhancing soil properties and mitigating climate change.

In summary, the present study advances the understanding of soil stabilization techniques and provides practical recommendations for achieving sustainable soil management practices. Future research efforts should focus on further elucidating the mechanisms underlying the observed effects of these soil additives on other soil types and exploring innovative approaches for enhancing soil carbon sequestration and sustainability.

5. Conclusions

The present study provides comprehensive investigations into the efficacy and sustainable stabilization of soft marine soils, focusing on the incorporation of MgO, biochar, and slag additives. Through a combination of laboratory experiments and rigorous analyses, the complex interplay between these additives and their impacts on soil hydraulic properties, carbon

sequestration potential, energy consumption, and economic feasibility are elucidated.

The study highlights the pivotal role of MIP analysis in revealing the underlying mechanisms driving CO₂ gas diffusion in stabilized soft marine soil subjected to accelerated carbonation. Significant alterations in pore structure across various treatment combinations were discerned through MIP, shedding light on the interplay between pore size distribution, carbon sequestration potential, and hydraulic properties of stabilized soils. MgO-based treatments demonstrate potential in enhancing soil stability and carbon sequestration, albeit with higher energy consumption and production costs. Specifically, MgO–biochar-treated samples exhibited enhanced pore volumes in inter-aggregate pores (0.01–0.05 μm), augmenting pore connectivity, surface reactivity, and carbon sequestration efficiency. Conversely, MgO–slag-treated samples demonstrated reduced pore volumes in larger pores, constraining CO₂ diffusion and carbonation product formation, resulting in larger pore volumes within the mesopore region (0.0028–0.01 μm). The findings highlight the promising carbon capture potential of MgO–biochar treatments, with significant hydration and carbonation products, such as brucite and nesquehonite, found in these formulations compared to the MgO–slag samples. Meanwhile, biochar could have facilitated the precipitation of hydration and carbonation phases by stimulating pozzolanic reactions, providing nucleation sites for chemical reactions, and enhancing gas diffusion through its porous matrix.

Furthermore, the sustainability assessment elucidates the trade-offs between environmental impact and economic feasibility, with MgO–biochar and MgO–slag combinations presenting cost-effective and more environmentally friendly alternatives to pure MgO treatments, highlighting the importance of holistic assessments, integrating environmental, economic, and engineering considerations.

Continued research efforts are advocated to optimize soil stabilization techniques, leveraging innovative approaches and emerging materials to enhance carbon sequestration efficiency while minimizing environmental footprint. In addition, due to the limitation of MIP in accurately estimating permeability, future studies could explore direct permeability measurements and integrate multiple characterization techniques for a more comprehensive assessment of material properties. The findings of this study offer insights for researchers, practitioners, and policymakers alike, advancing our understanding of sustainable soil management practices in line with global sustainability objectives.

Nomenclature

CaO	calcium oxide
CCUS	CO ₂ capture utilization and storage
CO ₂	carbon dioxide
CC	cumulative cost
CCO ₂	cumulative CO ₂ emissions
CEE	cumulative embodied energy
d	days



D	pore diameter
DMS	dredged marine soil
e	void ratio
h	hours
HMCs	hydrated magnesium carbonates
IPCC	intergovernmental panel on climate change
k	permeability
n	porosity
OPC	ordinary Portland cement
MgO	magnesium oxide
SAC	soil air content
SCMs	supplementary cementitious materials
SEM	scanning electron microscopy
W_{opt}	optimum water content
XRD	X-ray diffraction
γ_{dmax}	maximum dry density

Data availability

The data that support the findings of this study are available from the corresponding author upon reasonable request, or you can access from the sheets from the ESI information Excel file.†

Author contributions

Chikezie Chimere Onyekwena: conceptualization, methodology, investigation, visualization, writing – original draft & editing; Qi Li: project administration, supervision, visualization, writing – review, and funding acquisition; Yong Wang: resources, writing – review & editing; Ishrat Hameed Alvi: writing – review & editing; Yunlu Hou: writing – review & editing; Chima Finnian Ukaomah: methodology, writing – review & editing; Theogene Hakuzweyezu: writing – review & editing.

Conflicts of interest

The authors declare that they have no known competing financial interests or personal relationships that could have appeared to influence the work reported in this paper.

Acknowledgements

This work was supported by the Creative Groups of Natural Science Foundation of Hubei Province [Grant No. 2021CFA030]. Ishrat Hameed Alvi is a recipient of the 2021 PhD ANSO Scholarship. Theogene Hakuzweyezu is a recipient of the 2022 PhD ANSO Scholarship.

References

- Q. Li, Z. A. Chen, J. T. Zhang, L. C. Liu, X. C. Li and L. Jia, Positioning and revision of CCUS technology development in China, *Int. J. Greenhouse Gas Control*, 2016, **46**, 282–293, DOI: [10.1016/j.ijggc.2015.02.024](https://doi.org/10.1016/j.ijggc.2015.02.024).
- Y. M. Wei, J. N. Kang, L. C. Liu, Q. Li, P. T. Wang, J. J. Hou, Q. M. Liang, H. Liao, S. F. Huang and B. Yu, A proposed global layout of carbon capture and storage in line with a 2 °C climate target, *Nat. Clim. Change*, 2021, **11**, 112–118, DOI: [10.1038/s41558-020-00960-0](https://doi.org/10.1038/s41558-020-00960-0).
- I. H. Alvi, Q. Li, Y. Hou, C. C. Onyekwena, M. Zhang and A. Ghaffar, A critical review of cement composites containing recycled aggregates with graphene oxide nanomaterials, *J. Build. Eng.*, 2023, **69**, 105989, DOI: [10.1016/J.JOBE.2023.105989](https://doi.org/10.1016/J.JOBE.2023.105989).
- G. Cai, S. Liu, Y. Zhong, C. Poon and J. Li, Model investigation of the low-carbon MgO-treated soil foundation based on CO₂ overall carbonation, *J. Rock Mech. Geotech. Eng.*, 2023, **15**, 2901–2916, DOI: [10.1016/J.JRMGE.2023.02.018](https://doi.org/10.1016/J.JRMGE.2023.02.018).
- W. Li, Y. Chen, R. Li, H. Xiao, L. Li and J. Yang, A new method for carbonating magnesia and its possible application to soil stabilization and CO₂ capture, *Constr. Build. Mater.*, 2023, **383**, 131263, DOI: [10.1016/J.CONBUILDMAT.2023.131263](https://doi.org/10.1016/J.CONBUILDMAT.2023.131263).
- F. Jin, F. Wang and A. Al-Tabbaa, Three-year performance of in-situ solidified/stabilised soil using novel MgO-bearing binders, *Chemosphere*, 2016, **144**, 681–688, DOI: [10.1016/J.CHEMOSPHERE.2015.09.046](https://doi.org/10.1016/J.CHEMOSPHERE.2015.09.046).
- J. Wu, L. Liu, Y. Deng, G. Zhang, A. Zhou and H. Xiao, Use of recycled gypsum in the cement-based stabilization of very soft clays and its micro-mechanism, *J. Rock Mech. Geotech. Eng.*, 2022, **14**, 909–921, DOI: [10.1016/J.JRMGE.2021.10.002](https://doi.org/10.1016/J.JRMGE.2021.10.002).
- D. Wang, J. Zhu and F. He, CO₂ carbonation-induced improvement in strength and microstructure of reactive MgO-CaO-fly ash-solidified soils, *Constr. Build. Mater.*, 2019, **229**, 116914, DOI: [10.1016/j.conbuildmat.2019.116914](https://doi.org/10.1016/j.conbuildmat.2019.116914).
- C. C. Onyekwena, Q. Xue, Q. Li, H. I. Umeobi, A. Ghaffar and M. H. Fasihnikoutalab, Advances in the carbonation of MgO-based binder and CO₂ utilization in the construction industry, *Clean Technol. Environ. Policy*, 2023, **25**, 1763–1782, DOI: [10.1007/s10098-023-02482-7](https://doi.org/10.1007/s10098-023-02482-7).
- S. Ruan, T. Wang, R. Guo and C. Unluer, Assessment of the properties and environmental impact of carbonated reactive magnesia containing industrial waste, *Thermochim. Acta*, 2021, **706**, 179051, DOI: [10.1016/J.TCA.2021.179051](https://doi.org/10.1016/J.TCA.2021.179051).
- G. Cai, S. Liu, G. Du, Z. Chen, X. Zheng and J. Li, Mechanical performances and microstructural characteristics of reactive MgO-carbonated silt subjected to freezing-thawing cycles, *J. Rock Mech. Geotech. Eng.*, 2021, **13**, 875–884, DOI: [10.1016/J.JRMGE.2021.03.005](https://doi.org/10.1016/J.JRMGE.2021.03.005).
- L. Pu and C. Unluer, Effect of preconditioning on carbonated reactive MgO-based concrete samples, *J. Mater. Civ. Eng.*, 2020, **32**, 04020314, DOI: [10.1061/\(ASCE\)MT.1943-5533.0003416](https://doi.org/10.1061/(ASCE)MT.1943-5533.0003416).
- D. Wang, J. Zhu and F. He, Quantification and micro-mechanisms of CO₂ sequestration in magnesia-lime-fly ash/slag solidified soils, *Int. J. Greenhouse Gas Control*, 2019, **91**, 102827, DOI: [10.1016/j.ijggc.2019.102827](https://doi.org/10.1016/j.ijggc.2019.102827).
- N. T. Dung and C. Unluer, Improving the carbonation of reactive MgO cement concrete via the use of NaHCO₃ and NaCl, *J. Mater. Civ. Eng.*, 2018, **30**, 04018320, DOI: [10.1061/\(ASCE\)MT.1943-5533.0002509](https://doi.org/10.1061/(ASCE)MT.1943-5533.0002509).
- Y. Yi, M. Liska, F. Jin and A. Al-Tabbaa, Mechanism of reactive magnesia – ground granulated blastfurnace slag



- (GGBS) soil stabilization, *Can. Geotech. J.*, 2016, **53**, 773–782, DOI: [10.1139/cgj-2015-0183](https://doi.org/10.1139/cgj-2015-0183).
- 16 C. C. Onyekwena, Q. Li, I. H. Alvi, A. Ghaffar and X. Zhang, Geomechanical performances of geocell reinforced retaining wall backfilled with magnesia-based cement stabilized marine fill, *Mar. Georesour. Geotechnol.*, 2023, **42**, 617–633, DOI: [10.1080/1064119X.2023.2211060](https://doi.org/10.1080/1064119X.2023.2211060).
- 17 X. Zhu, X. Wang and Y. S. Ok, The application of machine learning methods for prediction of metal sorption onto biochars, *J. Hazard. Mater.*, 2019, **378**, 120727, DOI: [10.1016/J.JHAZMAT.2019.06.004](https://doi.org/10.1016/J.JHAZMAT.2019.06.004).
- 18 C. C. Onyekwena, Q. Xue, Q. Li, Y. Wan, S. Feng, H. I. Umeobi, H. Liu and B. Chen, Support vector machine regression to predict gas diffusion coefficient of biochar-amended soil, *Appl. Soft Comput.*, 2022, **127**, 109345, DOI: [10.1016/J.ASOC.2022.109345](https://doi.org/10.1016/J.ASOC.2022.109345).
- 19 T. Chen, L. Zhao, X. Gao, L. Li and L. Qin, Modification of carbonation-cured cement mortar using biochar and its environmental evaluation, *Cem. Concr. Compos.*, 2022, **134**, 104764, DOI: [10.1016/j.cemconcomp.2022.104764](https://doi.org/10.1016/j.cemconcomp.2022.104764).
- 20 H. Maljaee, R. Madadi, H. Paiva, L. Tarelho and V. M. Ferreira, Incorporation of biochar in cementitious materials: A roadmap of biochar selection, *Constr. Build. Mater.*, 2021, **283**, 122757, DOI: [10.1016/J.CONBUILDMAT.2021.122757](https://doi.org/10.1016/J.CONBUILDMAT.2021.122757).
- 21 Y. Zhang, M. He, L. Wang, J. Yan, B. Ma, X. Zhu, Y. S. Ok, V. Mechtcherine and D. C. W. Tsang, Biochar as construction materials for achieving carbon neutrality, *Biochar*, 2022, **4**, 1–25, DOI: [10.1007/S42773-022-00182-X](https://doi.org/10.1007/S42773-022-00182-X).
- 22 C. C. Onyekwena, Q. Li, Y. Wang, I. H. Alvi, W. Li, Y. Hou, X. Zhang and M. Zhang, Dredged marine soil stabilization using magnesia cement augmented with biochar/slag, *J. Rock Mech. Geotech. Eng.*, 2024, **16**, 1000–1017, DOI: [10.1016/J.JRMGE.2023.05.005](https://doi.org/10.1016/J.JRMGE.2023.05.005).
- 23 F. Q. Chen, N. K. Zhao, S. Feng, H. W. Liu and Y. C. Liu, Effects of biochar content on gas diffusion coefficient of soil with different compactness and air contents, *Environ. Sci. Pollut. Res.*, 2020, **27**, 21497–21505, DOI: [10.1007/S11356-020-08594-7](https://doi.org/10.1007/S11356-020-08594-7).
- 24 X. Ma, Y. Du, C. Fu, H. Fang, H. Wei, Z. Pan, S. Sang and J. Zhang, Effects of supercritical CO₂ on the pore structure complexity of high-rank coal with water participation and the implications for CO₂ ECBM, *ACS Omega*, 2023, **8**, 18964–18980, DOI: [10.1021/acsomega.3c01486](https://doi.org/10.1021/acsomega.3c01486).
- 25 C. F. Ukaomah, L. Zhang, Y. Xu, M. Sun, B. Yang, A. I. Madaki, H. I. Umeobi and M. D. Aminu, Pore structure and seal capacity of Ilaro formation shales in the Eastern Dahomey basin: Implications from mercury injection capillary pressure and spontaneous imbibition analyses, *Energy Fuels*, 2021, **35**, 10086–10101, DOI: [10.1021/ACS.ENERGYFUELS.1C01153](https://doi.org/10.1021/ACS.ENERGYFUELS.1C01153).
- 26 W. Li, Y. Yi and A. J. Puppala, Comparing carbide sludge-ground granulated blastfurnace slag and ordinary Portland cement: Different findings from binder paste and stabilized clay slurry, *Constr. Build. Mater.*, 2022, **321**, 126382, DOI: [10.1016/J.CONBUILDMAT.2022.126382](https://doi.org/10.1016/J.CONBUILDMAT.2022.126382).
- 27 L. Lang, B. Chen and B. Chen, Strength evolutions of varying water content-dredged sludge stabilized with alkali-activated ground granulated blast-furnace slag, *Constr. Build. Mater.*, 2021, **275**, 122111, DOI: [10.1016/J.CONBUILDMAT.2020.122111](https://doi.org/10.1016/J.CONBUILDMAT.2020.122111).
- 28 A. R. Estabragh, A. Jahani, A. A. Javadi and M. Babalar, Assessment of different agents for stabilisation of a clay soil, *Int. J. Pavement Eng.*, 2020, **23**, 160–170, DOI: [10.1080/10298436.2020.1736293](https://doi.org/10.1080/10298436.2020.1736293).
- 29 E. W. Washburn, The dynamics of capillary flow, *Phys. Rev.*, 1921, **17**, 273–283, DOI: [10.1103/PhysRev.17.273](https://doi.org/10.1103/PhysRev.17.273).
- 30 G. H. Cai, Y. J. Du, S. Y. Liu and D. N. Singh, Physical properties, electrical resistivity, and strength characteristics of carbonated silty soil admixed with reactive magnesia, *Can. Geotech. J.*, 2015, **52**, 1699–1713, DOI: [10.1139/cgj-2015-0053](https://doi.org/10.1139/cgj-2015-0053).
- 31 T. T. Nguyen, A. Demortière, B. Fleutot, B. Delobel, C. Delacourt and S. J. Cooper, The electrode tortuosity factor: Why the conventional tortuosity factor is not well suited for quantifying transport in porous Li-ion battery electrodes and what to use instead, *npj Comput. Mater.*, 2020, **6**, 1–12, DOI: [10.1038/s41524-020-00386-4](https://doi.org/10.1038/s41524-020-00386-4).
- 32 S. J. Cooper, A. Bertei, P. R. Shearing, J. A. Kilner and N. P. Brandon, TauFactor: An open-source application for calculating tortuosity factors from tomographic data, *SoftwareX*, 2016, **5**, 203–210, DOI: [10.1016/J.SOFTX.2016.09.002](https://doi.org/10.1016/J.SOFTX.2016.09.002).
- 33 ISO 14040, *Environmental Management: Life Cycle Assessment — Principles and Framework*, Geneva, Switzerland, 2006. <https://www.iso.org/standard/37456.html>, accessed January 30, 2024.
- 34 J. Rouquerol, G. Baron, R. Denoyel, H. Giesche, J. Groen, P. Klobes, P. Levitz, A. V. Neimark, S. Rigby, R. Skudas, K. Sing, M. Thommes and K. Unger, Liquid intrusion and alternative methods for the characterization of macroporous materials (IUPAC technical report), *Pure Appl. Chem.*, 2012, **84**, 107–136, DOI: [10.1351/PAC-REP-10-11-19](https://doi.org/10.1351/PAC-REP-10-11-19).
- 35 Z. Gao and Q. Hu, Estimating permeability using median pore-throat radius obtained from mercury intrusion porosimetry, *J. Geophys. Eng.*, 2013, **10**, 25014–25021, DOI: [10.1088/1742-2132/10/2/025014](https://doi.org/10.1088/1742-2132/10/2/025014).
- 36 X. Dai, L. Lian, X. Jia, J. Qin and J. Qian, Preparation and properties of magnesium phosphate cement with recycled magnesia from waste magnesia refractory bricks, *J. Build. Eng.*, 2023, **63**, 105491, DOI: [10.1016/J.JOBE.2022.105491](https://doi.org/10.1016/J.JOBE.2022.105491).
- 37 B. O. Adeleke, J. M. Kinuthia and J. E. Oti, Impacts of MgO waste: GGBS formulations on the performance of a stabilised natural high sulphate bearing soil, *Constr. Build. Mater.*, 2022, **315**, 125745, DOI: [10.1016/J.CONBUILDMAT.2021.125745](https://doi.org/10.1016/J.CONBUILDMAT.2021.125745).
- 38 A. Loudini, M. Ibnoussina, O. Witam, A. Limam and O. Turchanina, Valorisation of dredged marine sediments for use as road material, *Case Stud. Constr. Mater.*, 2020, **13**, e00455, DOI: [10.1016/J.CSCM.2020.E00455](https://doi.org/10.1016/J.CSCM.2020.E00455).
- 39 S. Y. Liu, G. H. Cai, G. Y. Du, L. Wang, J. S. Li and X. C. Qian, Field investigation of shallow soft-soil highway subgrade treated by mass carbonation technology, *Can. Geotech. J.*, 2021, **58**, 97–113, DOI: [10.1139/cgj-2020-0008](https://doi.org/10.1139/cgj-2020-0008).

